

Measurement of structure dependent radiative $K^+ \rightarrow e^+\nu\gamma$ decays using stopped positive kaons

H. Ito,^{1,*} A. Kobayashi,¹ S. Bianchin,² T. Cao,³ C. Djalali,⁴ D.H. Dongwi,³
T. Gautam,³ D. Gill,² M. D. Hasinoff,⁵ K. Horie,⁶ Y. Igarashi,⁷ J. Imazato,⁷
N. Kalantarians,^{3,†} H. Kawai,¹ S. Kimura,¹ S. Kodama,¹ M. Kohl,³
H. Lu,⁴ O. Mineev,⁸ P. Monaghan,^{3,‡} S. Shimizu,^{6,§} S. Strauch,⁹
M. Tabata,¹ R. Tanuma,^{10,¶} A. Toyoda,⁷ H. Yamazaki,⁷ and N. Yershov⁸

(J-PARC E36 Collaboration)

¹*Department of Physics, Chiba University, Chiba, 263-8522, Japan*

²*TRIUMF, Vancouver, BC, V6T 2A3, Canada*

³*Physics Department, Hampton University, VA 23668, USA*

⁴*Department of Physics and Astronomy,
University of Iowa, Iowa City, IA 52242, USA*

⁵*Department of Physics and Astronomy,
University of British Columbia, Vancouver, BC, V6T 1Z1, Canada*

⁶*Department of Physics, Osaka University, Osaka, 560-0043, Japan*

⁷*High Energy Accelerator Research Organization (KEK), Tsukuba, 305-0801, Japan*

⁸*Institute for Nuclear Research, Moscow, 117312, Russia*

⁹*Department of Physics, University of South Carolina, USA*

¹⁰*Department of Physics, Rikkyo University, Toshima, 171-8501, Japan*

The structure dependent radiative $K^+ \rightarrow e^+\nu\gamma$ ($K_{e2\gamma}^{\text{SD}}$) decay was investigated with stopped positive kaons. The e^+ momentum spectra were measured with and without a photon in coincidence and analyzed with Monte Carlo simulations for acceptance and detector response to extract the ratio of the $K_{e2\gamma}^{\text{SD}}$ and $K^+ \rightarrow e^+\nu$ (K_{e2}) branching ratios. A value of $Br(K_{e2\gamma}^{\text{SD}})/Br(K_{e2}) = 1.22 \pm 0.07_{\text{stat}} \pm 0.04_{\text{syst}}$ was obtained, which is significantly larger than the value inferred from a previous experimental result for $Br(K_{e2\gamma}^{\text{SD}})/Br(K^+ \rightarrow \mu^+\nu)$.

* Present address: Department of Physics, Tokyo University of Science, Noda, Chiba 278-8510, Japan.

† Present address: Department of Natural Sciences, Virginia Union University, Richmond VA 23220, USA

‡ Present address: Department of Physics, Christopher Newport University, Newport News, VA 23606, USA

High precision measurements of electroweak observables represent powerful tests of the Standard Model (SM) to obtain hints of new physics [1]. The $K^+ \rightarrow l^+\nu_l$ decay, which is the simplest semileptonic decay among the K^+ decay channels, is a clean and sensitive channel to perform such tests. Lepton universality signifies the identical coupling constants of the three lepton generations, and is a basic assumption in the SM. Although each K_{l2} decay width can be described using the K_{l2} hadronic form factor with a few percent accuracy, this form factor can be canceled out by forming the ratio of the electric $K^+ \rightarrow e^+\nu$ (K_{e2}) and muonic $K^+ \rightarrow \mu^+\nu$ ($K_{\mu2}$) decay channels (R_K).

In the R_K determination, the radiative $K^+ \rightarrow e^+\nu\gamma$ decay ($K_{e2\gamma}$), which is the K_{e2} decay accompanied with photon emission, has to be taken into account. There are two $K_{e2\gamma}$ processes [2, 3]: the internal bremsstrahlung (IB) process, $K_{e2\gamma}^{\text{IB}}$, mostly with low-energy photon emission and the structure dependent (SD) process, $K_{e2\gamma}^{\text{SD}}$, with high-energy photon emission roughly in the same and opposite directions of the e^+ motions, respectively. In order to compare the experimental value with the SM prediction, the IB process has to be included in the K_{e2} sample because it is impossible to experimentally separate the IB process from the K_{e2} decay. The SM prediction, $R_K^{\text{SM}} = (2.477 \pm 0.001) \times 10^{-5}$, can be calculated with excellent accuracy [4–7], and this makes it possible to search for new physics effects by a precise R_K measurement [8, 9]. On the other hand, the SD process, which has a large hadronic uncertainty, is regarded as a background and has to be subtracted from the observed K_{e2} events. The K_{e2} branching ratio is strongly suppressed down to $\sim 10^{-5}$ due to the helicity suppression mechanism of the weak charged current. The SD process is not subject to the above helicity suppression, and the branching $K_{e2\gamma}^{\text{SD}}$ ratio is comparable to that of K_{e2} . The SD process is sensitive to the electroweak structure of the kaon and has been the subject of extensive theoretical studies [2, 3, 10, 11].

The KLOE [8] and NA62 [9] groups have reported experimental results for R_K . In the most recent NA62 experiment which produced the result with the smallest uncertainty, in-flight kaon decays in a beam of particle momenta from 15 to 65 GeV/ c were used, and the $K_{\mu2}$ and $K_{e2\gamma}^{\text{SD}}$ decays were the main background sources in the K_{e2} sample. On the other hand, low energy kaons from $\phi \rightarrow K^+K^-$ decays were used in the preceding KLOE experiment. The kinematic resolution of K_{l2} decay was better than that in NA62, however the experimental result was dominated by the statistical uncertainty. The NA62 and KLOE

§ Corresponding author: suguru@phys.sci.osaka-u.ac.jp

¶ Deceased

results were obtained to be $R_K = (2.488 \pm 0.007_{\text{stat}} \pm 0.007_{\text{sys}}) \times 10^{-5}$ and $R_K = (2.493 \pm 0.025_{\text{stat}} \pm 0.019_{\text{sys}}) \times 10^{-5}$, respectively, which are consistent with the SM prediction within the uncertainties. It should be noted that the branching ratio of the $K_{e2\gamma}^{\text{SD}}$ reported by the KLOE group was used in the NA62 analysis, and this SD contribution was subtracted from the observed K_{e2} samples. Therefore, an experimental check of the SD branching ratio with a systematically different approach from KLOE is important. In this letter, we present a new measurement of the branching ratio of the $K_{e2\gamma}^{\text{SD}}$ decay relative to that of the K_{e2} decay, $\text{Br}(K_{e2\gamma}^{\text{SD}})/\text{Br}(K_{e2})$, performed with the J-PARC E36 experiment, which is also aiming at testing lepton universality violation with a precise R_K measurement [12, 13]. In contrast to the previous R_K measurements, the E36 experiment used a stopped K^+ beam in conjunction with a 12-sector iron-core superconducting toroidal spectrometer [14] and a highly segmented CsI(Tl) calorimeter [15]. Schematic cross sectional side and end views of the detector configuration are shown in Fig. 1. Because of the rotational symmetry of the 12 identical gaps in the spectrometer and the large directional acceptance of the π^0 detector, spectra distortions due to detector acceptance are cancelled and systematic uncertainties are greatly suppressed [16]. The experimental apparatus was originally constructed for the KEK-PS E246/E470 experiments: a search for T -violating muon polarization in $K^+ \rightarrow \pi^0 \mu^+ \nu$ decay [17] and spectroscopic studies of various K^+ decay channels [18].

The experiment was performed at the J-PARC Hadron Experimental Facility using a 780 MeV/ c separated K^+ beam provided by the K1.1BR beam line with a K/π ratio of ~ 1 . The K^+ beam was discriminated from pion background by a Fitch-type Cherenkov counter (BC) [19]. An efficiency of more than 99% with a small π mis-trigger probability of $< 1\%$ was achieved for the K^+ identification. The typical K^+ beam intensity was 1×10^6 in a 2-s spill duration and 6-s repetition rate. The kaons were slowed down by a degrader and stopped in an active target (TGT), which consisted of 256 3.1×3.1 mm² thin scintillating bars of 20-cm length forming a cylindrical bundle with a 5.6-cm diameter, located at the center of the detector assembly. The K^+ stopping efficiency was typically ~ 0.25 relative to BC K^+ triggering, and the K^+ stopping profile had a round shape with a Gaussian-like distribution with σ_z of ~ 4 cm in the beam direction.

$K_{e2\gamma}$ and K_{e2} events were identified by analyzing the e^+ momentum (p) with the 12-sector spectrometer taken under the same trigger and DAQ conditions and, in addition, detecting the photon in the CsI(Tl) calorimeter for $K_{e2\gamma}$. The data were collected at a central magnetic field of $B = 1.5$ T, which was optimized for the positron momenta in

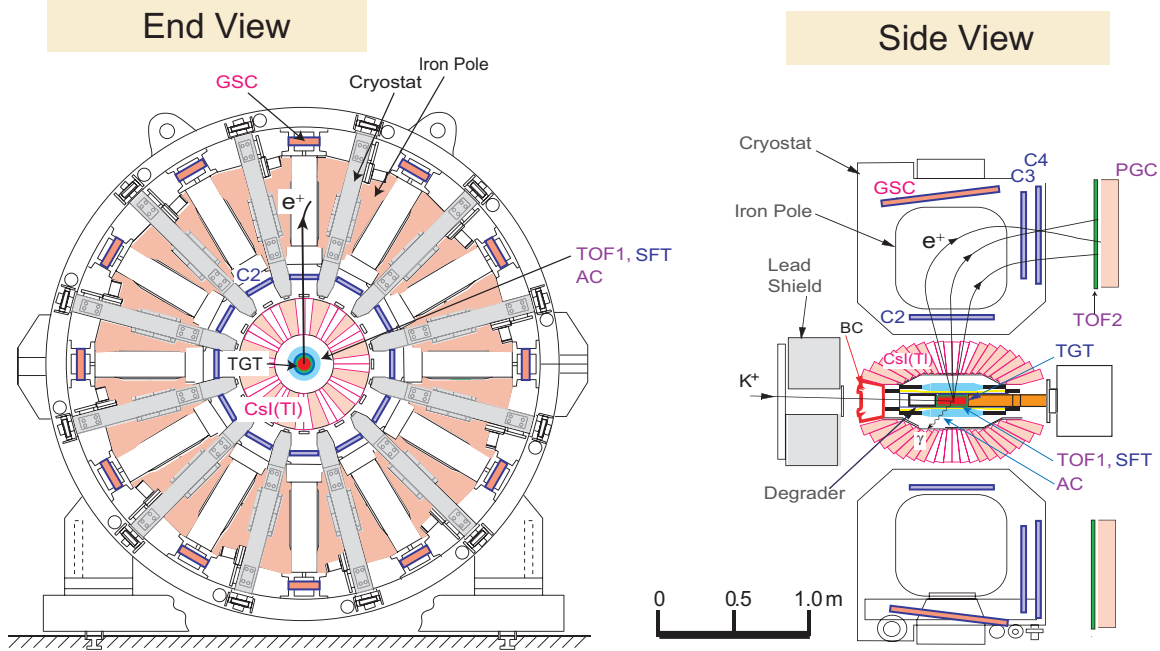


FIG. 1. Schematic cross sectional side view (right) and end view (left) of the E36 detector configuration. Charged particles from TGT were momentum-analyzed by reconstructing the particle trajectory using three MWPCs, C2, C3, and C4, as well as by TGT and SFT. Particle identification was carried out using AC, PGC and by measuring the time-of-flight between the TOF1 and TOF2 counters. The photon energy and hit position were measured by the CsI(Tl) calorimeter.

the region of 220–250 MeV/ c . Charged particles from TGT were tracked and momentum-analyzed by reconstructing the particle trajectory using multi-wire proportional chambers (MWPCs) located at the entrance (C2) and exit (C3 and C4) of the magnet gap, as well as by TGT and spiral fiber tracker (SFT) made of scintillating fiber bundles [20, 21] surrounding TGT. The momentum was corrected for the energy loss in TGT assuming that all particles were muons, therefore the π^+ and e^+ momenta after the correction were slightly shifted from their true values. The momentum spectrum before imposing the PID analysis is shown in Fig. 2 (a). Two peaks due to the $K_{\mu 2}$ and $K^+ \rightarrow \pi^+\pi^0$ ($K_{\pi 2}$) decays are clearly visible. The momentum resolution is obtained to be $\sigma_p = 2.0$ MeV/ c at 236 MeV/ c . The K^+ decay time, defined as the e^+ signal at the TOF1 counter, was required to be more than 1.5 ns later than the K^+ arrival time determined by BC. Small time-of-flight corrections from BC to TGT, and TGT to TOF1 were accounted for on average. This reduced the fraction of in-flight K^+ decays and any other prompt backgrounds to a negligible level.

Particle identification (PID) of μ^+ , π^+ , and e^+ was carried out in each of the 12 sectors

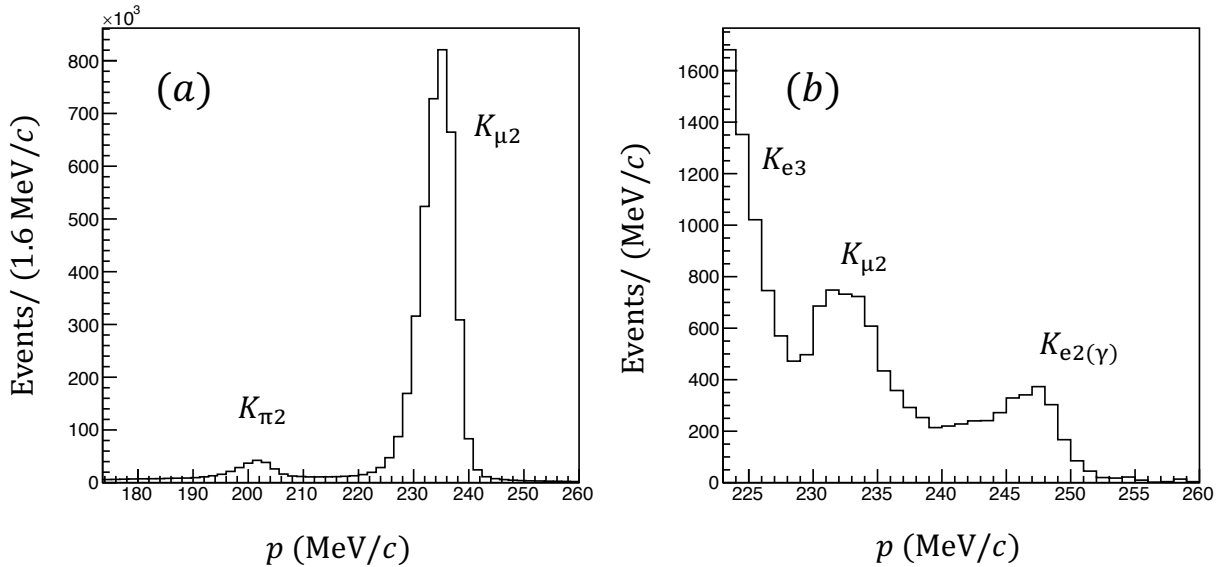


FIG. 2. (a) and (b) are the momentum spectra corrected for the energy loss in TGT before and after imposing the positron selection PID, respectively. The peak structure due to the predominant $K_{\mu 2}$ and $K_{\pi 2}$ decays is seen at 236 MeV/c and 205 MeV/c, respectively, in (a). The $K_{e 2(\gamma)}$ and $K_{e 3}$ decays, as well as the remaining $K_{\mu 2}$ events due to μ^+ mis-identification are presented in (b). The $K_{e 2}$ peak is observed with a tail structure in the lower momentum region due to the emission of internal and external bremsstrahlung before entering the spectrometer. The momentum in (b) was scaled so that $K_{e 2}$ peak position is at 247 MeV/c, and consequently the $K_{\mu 2}$ peak position appears at 233 MeV/c.

using an aerogel Cherenkov counter (AC) [22], a lead-glass Cherenkov counter (PGC) [23], and by measuring the time-of-flight (TOF) between the TOF1 and TOF2 plastic scintillation counters. The AC and TOF1 surrounded TGT while TOF2 was located about 90 cm behind C4. The PGC was placed just after TOF2 at the end of the spectrometer. Figure 3 shows the e^+ efficiency (solid/red) and the μ^+ rejection probability (dotted/black) at the momentum of 247 MeV/c and 236 MeV/c, respectively, as functions of the (a) AC, (b) PGC, and (c) M_{TOF}^2 cut points. The e^+ efficiency was obtained by pre-selecting e^+ from the $K^+ \rightarrow \pi^0 e^+ \nu$ ($K_{e 3}$) and in-flight $K_{e 3}$ decays for the momentum region higher than the $K_{e 3}$ endpoint momentum (228 MeV/c) by keeping the other two PID conditions at their selected values. Since the pulse height of the PGC counter increased with increasing e^+ momentum, this introduced a momentum dependence in the PGC detection efficiency. The PGC efficiency curve from 200 to 250 MeV/c was measured to correct this effect. The

μ^+ rejection probability was determined using μ^+ s from the $K_{\mu 2}$ decays. Positrons were selected by setting thresholds for AC and PGC at channel 100 and 140, respectively. Also, the mass-squared of the charged particle (M_{TOF}^2) obtained from the TOF, momentum, and path length was required to be $M_{\text{TOF}}^2 < 4000$ (MeV^2/c^4). These positron selection cuts, as shown in Fig. 3, were chosen to remove most of the $K_{\mu 2}$ backgrounds with a μ^+ rejection probability of $>99.9\%$, while keeping a reasonable e^+ efficiency of 76% . This was determined to minimize the total uncertainty in the $K_{e2\gamma}$ branching ratio measurement from the $K_{\mu 2}$ subtraction. Figure 2 (b) shows the charged-particle momentum spectrum with the positron PID condition applied. The K_{e2} , $K_{e2\gamma}$, and K_{e3} decays, as well as the remaining $K_{\mu 2}$ events due to μ^+ mis-identification are presented, where the momentum was slightly scaled so that the K_{e2} peak position is at 247 MeV/c . The K_{e2} peak has a tail structure in the lower momentum region mainly due to the emission of external bremsstrahlung before entering the spectrometer.

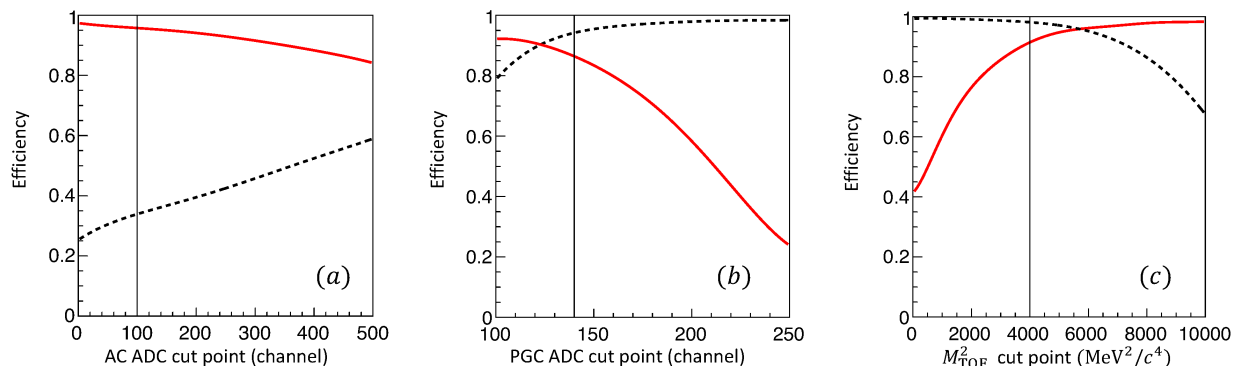


FIG. 3. The e^+ detection efficiency (solid/red lines) and μ^+ rejection probability (dashed/black lines), as functions of the (a) AC, (b) PGC, and (c) M_{TOF}^2 cut points. The cut points adopted for each detector are also shown, and for the measurement of the each element, the other two of these cut points were used.

The photon detector, an assembly of 768 CsI(Tl) crystals, covered $\sim 70\%$ of the total solid angle. There were 12 holes for outgoing charged particles to enter the spectrometer and 2 holes for the beam entrance and exit. Each crystal has a length of 25 cm and covers 7.5° in both the polar and azimuthal direction. The photon energy and hit position were obtained by summing the energy deposits and calculating the energy-weighted centroid of participating crystals in the Moliere spread. To read out the CsI(Tl) calorimeter, VF48 Flash ADCs [24] were employed to record the waveform data in order to resolve pulse-

pileup events with high efficiency. The hardware threshold was set at ~ 17 MeV to limit the event size. The CsI(Tl) energy and timing resolutions of a single module at 105 MeV were $\sigma_E/E \approx 2.6\%$ and $\sigma_t = 10.7$ ns [25], respectively, and the position resolution was obtained as $\sigma_{\text{pos}} = 7.6$ mm. Accidental backgrounds were reduced by choosing a timing window of ± 50 ns. In addition, some of the photons that passed through the holes in the CsI(Tl) calorimeter into the spectrometer sectors were detected by gap shower counters (GSC), which are sandwich detectors of plastic scintillators and lead plates that will allow us to perform future $K_{e2\gamma}$ studies.

In the present study, the SD branching ratio, $Br(K_{e2\gamma}^{\text{SD}})$ normalized to that of K_{e2} decay, $Br(K_{e2})$, was determined from the ratio of the $K_{e2\gamma}$ and K_{e2} yields, corrected for the detector acceptance as,

$$\frac{Br(K_{e2\gamma}^{\text{SD}})}{Br(K_{e2})} = \frac{N(K_{e2\gamma}^{\text{SD}})}{N(K_{e2})} \cdot R_\Omega = \frac{N(K_{e2\gamma}^{\text{SD}})}{N(K_{e2})} \cdot \frac{\Omega(K_{e2})}{\Omega(K_{e2\gamma})}, \quad (1)$$

where N is the number of the accepted events and R_Ω is the ratio of the overall acceptances Ω for K_{e2} and $K_{e2\gamma}^{\text{SD}}$, respectively, obtained by a Monte Carlo simulation. In contrast to the previous KLOE experiment which determined $Br(K_{e2\gamma}^{\text{SD}})$ relative to $Br(K_{\mu 2})$, the present experiment was able to disentangle both the number of $N(K_{e2})$ and $N(K_{e2\gamma}^{\text{SD}})$ events directly from the charged particle momentum spectra. The spectrum in Fig. 2(b) was decomposed by simulating the spectrum of each contributing process and fitting the linear combination to the measured spectrum. In addition, $Br(K_{e2\gamma}^{\text{SD}})$ was further constrained with the data where a photon was detected in coincidence with the CsI(Tl) calorimeter. Our method has the following advantages: (1) charged particles from the K_{e2} and $K_{e2\gamma}$ decays are e^+ with very similar momenta, and the PID efficiency up to a small p dependence cancels out, (2) since the K_{e2} decay produces a peak at 247 MeV/ c in the momentum spectrum, as shown in Fig. 2 (b), the K_{e2} yield can be correctly determined, and the K_{e2} events can be easily suppressed by requiring a photon hit in the CsI(Tl) calorimeter for the $K_{e2\gamma}$ selection, (3) the CsI(Tl) acceptance can be determined using the two photons from the $K_{\pi 2}$ decay, (4) other systematic uncertainties from imperfect reproducibility of the experimental conditions such as tracker inefficiencies, detector misalignment, DAQ deadtime, etc. are also cancelled out in the ratio determination.

The detector acceptance for the $K_{e2\gamma}$ decays was calculated by a GEANT4-based Monte Carlo simulation assuming the theoretical scheme of vector and axial-vector transitions [2, 3].

The simulation data were generated assuming the Dalitz density given as,

$$\frac{d^2\Gamma(K_{e2\gamma}, \text{SD})}{dx dy} = \frac{G_F^2 \alpha m_K^5 \sin^2 \theta_c}{64\pi^2} \times [(V + A)^2 f_{\text{SD}^+} + (V - A)^2 f_{\text{SD}^-}], \quad (2)$$

where G_F is the Fermi constant, α is the fine structure constant, m_K is the kaon mass, and θ_c is the Cabibbo angle. The form factors V and A represent the vector and axial-vector transitions, respectively. The kinematical density distribution for both helicity terms f_{SD^+} and f_{SD^-} can be described as,

$$f_{\text{SD}^+} = (x + y - 1)^2(1 - x) \quad \text{and} \quad f_{\text{SD}^-} = (1 - y)^2(1 - x), \quad (3)$$

by ignoring small $\mathcal{O}(m_e/m_K)$ contributions, where $x = 2E_\gamma/m_K$ and $y = 2E_e/m_K$ are dimensionless photon and e^+ energies, respectively, and m_e is the positron mass. It should be noted that the SD^- , IB, and IB/ SD^+ interference are negligibly small in the high-momentum e^+ region $200 < p < 250$ MeV/ c [2]. Here, V was assumed to have the momentum transfer dependence $V = V_0[1 + \lambda(1 - x)]$, while A was constant, according to the Chiral Perturbation theory (ChPT) model at $\mathcal{O}(p^6)$ [10, 11]. The λ parameter was taken to be $\lambda = 0.3 \pm 0.1$, which is the current theoretical conceivable range of ChPT $\mathcal{O}(p^6)$ model calculations [3]. The K_{e2} and $K_{\mu 2}$ decays were also generated using the same simulation code.

Since the CsI(Tl) calorimeter surrounded the beam axis and it was exposed to a high rate of scattered beam particles, accidental backgrounds in the calorimeter contributed to the raw $K_{e2\gamma}$ event samples. This accidental background was taken into account in the simulation to reproduce the actual experimental conditions. We used the experimental background events and merged them with the simulation data, as follows. Since the $K_{\mu 2}$ decays with $p_\mu = 236$ MeV/ c did not have accompanying photons, the CsI(Tl) signals which coincide with the $K_{\mu 2}$ decays within the timing window of ± 50 ns can be treated as pure accidental backgrounds. The fraction of the radiative $K^+ \rightarrow \mu^+ \nu \gamma$ decay is negligibly small and causes no effect in this background study. The $K_{\mu 2}$ events were selected only by the momentum and PID analyses, and these CsI(Tl) signals were merged with the simulation data of the $K_{e2\gamma}$, K_{e2} , and $K_{\mu 2}$ decays. It should be noted that the ratio of the single-cluster and zero-cluster $K_{\mu 2}$ events was $\epsilon \sim 18\%$. The validity of this simulation method was checked using two photons ($E_{\gamma 1} > E_{\gamma 2}$) from the π^0 decay in $K^+ \rightarrow \pi^+ \pi^0$ tagged by the π^+ with $200 < p_\pi < 210$ MeV/ c and the photon energy higher than 21 MeV. Also, events with large shower leakage from the calorimeter were rejected by requiring $E_{\gamma 1} + E_{\gamma 2} > 120$ MeV. Figure 4 shows the experimental spectra (dots) of (a) $E_{\gamma 1}$, (b) $E_{\gamma 2}$, (c) opening angle

between the two photons, and (d) invariant mass ($M_{\gamma\gamma}$), together with the simulation data. The contribution from the π^0 decay and events with at least one accidental background hit in the two clusters are shown as the dashed (blue) and dotted (green) histograms, respectively. The solid (red) histogram is obtained by summing the two components and normalizing to the experimental yield. The simulation calculations are in good agreement with the experimental data, which indicates a good understanding of the photon measurement by the CsI(Tl) calorimeter. Also, the detection efficiencies of each CsI(Tl) module were determined using the above K_{π^2} events. Using the information of π^+ and one of the two photons, the second photon energy and direction were calculated, and the existence of the actual photon cluster was checked.

In order to select the $K_{e2\gamma}$ events, remove the K_{e2} events, and suppress the $K_{\mu 2}$ background events, photon hits in the CsI(Tl) calorimeter were required. Due to pile-up of the accidental backgrounds in the CsI(Tl), the accepted $K_{e2\gamma}$ events included 2-cluster events in the calorimeter with a ratio of ϵ compared with 1-cluster events. Since event loss in the 1-cluster data and the appearance of the 2-cluster events were taken into account in the simulation, the $K_{e2\gamma}$ branching ratio can be derived by comparing the experimental data with the simulation for both the 1-cluster and 2-cluster events simultaneously.

The $K_{e2\gamma}$ decays with 1-cluster in the CsI(Tl) were obtained using the following procedure. The photon energy and the opening angle between the e^+ and γ were required to be $E_\gamma > 21$ MeV and $\cos\theta_{e\gamma} < -0.8$. This E_γ cut point was a little higher than the hardware threshold to remove effects from small gain variations of each CsI(Tl) module. Assuming the $K^+ \rightarrow e^+\nu\gamma$ decay kinematics, the missing-mass-squared was calculated as $M_{\text{miss}}^2 = (m_K - E_e - E_\gamma)^2 - (\mathbf{p}_e + \mathbf{p}_\gamma)^2$ where \mathbf{p} is the momentum vector. The accepted interval was imposed to be $-4000 < M_{\text{miss}}^2 < 8000$ MeV²/c⁴. The momentum spectrum is shown in Fig. 5 (a) indicated by the dots. Here, a small contribution from $K_{\mu 2}$ with an accidental hit remained after the $K_{e2\gamma}$ selection cuts. The $K_{e2\gamma}$ decays obtained in the 2-cluster data were selected in a similar manner. If one of the two clusters satisfied the conditions for the 1-cluster analysis, the event was adopted as a $K_{e2\gamma}$ decay and the associated CsI(Tl) cluster was chosen as the true photon event, as shown in Fig. 5 (b). It should be noted that the $K_{\mu 2}$ surviving fraction relative to the $K_{e2\gamma}$ yield in the 2-cluster data is approximately twice that observed in the 1-cluster data because there are two photon candidates in the 2-cluster analysis.

The $Br(K_{e2\gamma}^{\text{SD}})/Br(K_{e2})$ value was obtained to be 1.24 ± 0.07 by simultaneously fitting the

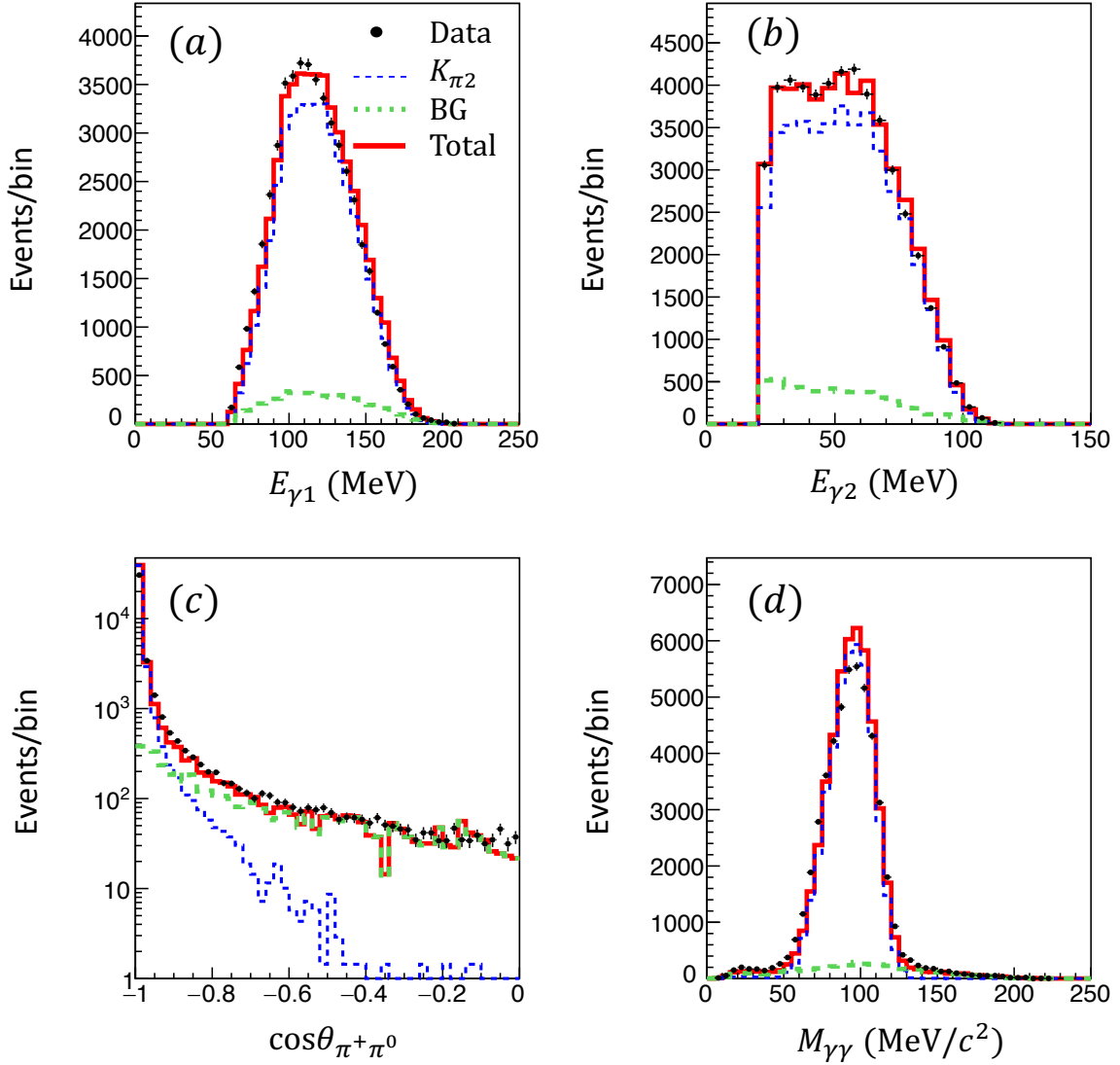


FIG. 4. $K_{\pi 2}$ spectra compared with the MC simulation taking into account the accidental backgrounds in the CsI(Tl) calorimeter. (a) and (b) are the photon energy distributions ($E_{\gamma 1} > E_{\gamma 2}$), (c) is the opening angle between the π^+ and π^0 , and (d) is the invariant mass $M_{\gamma\gamma}$. The black dots are the experimental data. The contribution from the π^0 decay and events with at least one of the two clusters being accidental are shown as the dashed (blue) and dotted (green) histograms, respectively, and the solid (red) histogram is obtained by summing the two components.

momentum spectra of the events with 1-cluster, 2-cluster, and without CsI(Tl) constraint using the simulation data of the $K_{e2\gamma}$, K_{e2} , and $K_{\mu 2}$ decays, as shown in Fig. 5 (a)(b)(c). The solid (green), dotted (blue), and dashed-dotted (magenta) lines are the decomposed $K_{e2\gamma}$, K_{e2} , and $K_{\mu 2}$ events. The thick-red line is the fitted result obtained by adding all the decay

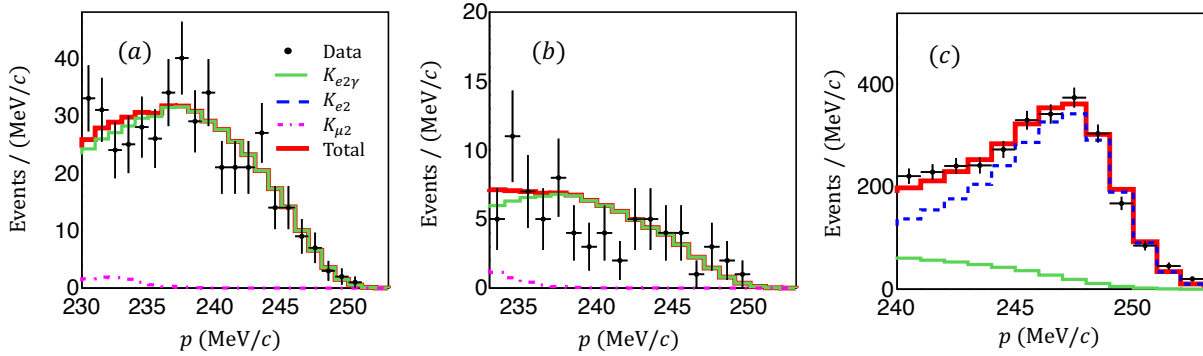


FIG. 5. Charged-particle momentum spectra with requiring (a) one photon cluster and (b) two photon clusters in coincidence with the e^+ track, and (c) charged particles without CsI(Tl) constraints. The dots (black) are the experimental data. The solid (green), dashed (blue), and dashed-dotted (magenta) lines are the $K_{e2\gamma}$, K_{e2} , and $K_{\mu2}$ decays, respectively, determined by simulation calculations. The thick-red lines are the fitted result obtained by adding all the decay contributions. The events are shown only for the fitted momentum range.

contributions. The fitting regions of $p > 230$, 232, and 240 MeV/ c for the events with 1-cluster, 2-cluster, without CsI(Tl) constraint, respectively, were adjusted to reduce the effects from the $K_{\mu2}$ subtraction by eliminating most of the $K_{\mu2}$ events. The $Br(K_{e2\gamma}^{SD})/Br(K_{e2})$ result as well as the accepted $K_{e2\gamma}$ and K_{e2} yields and the associated R_{Ω} values are given in Table I entitled as Run 1.

The events in Fig. 5 (a) were used for an event selection validity check. Figure 6 shows the distribution of (a) E_{γ} , (b) $\cos\theta_{e\gamma}$, and (c) M_{miss}^2 . The $K_{\mu2}$ background fraction in Fig. 6 was successfully suppressed down to $\sim 2\%$ of the $K_{e2\gamma}$ yield. The experimental data (dots) are in good agreement with the simulation (thick-solid/red), indicating a correct understanding of the $K_{e2\gamma}$ acceptance. The decomposed $K_{e2\gamma}$ (solid/green) and $K_{\mu2}$ (dashed-dotted/magenta) contributions are also shown.

In this experimental study, one of the key issues is the treatment of the accidental backgrounds in the CsI(Tl) calorimeter and the $K_{\mu2}$ backgrounds that survive after the PID analysis. In order to validate this analysis method, systematic-control data (Run 2) were taken under non-optimum beamline conditions as well as by changing the PID detector settings to increase the $K_{\mu2}$ background events. As a result, the surviving $K_{\mu2}$ fraction in the Run 2 data was a factor of ~ 3 higher than that in the Run 1 data. These data samples were independently analyzed using the same analysis codes adopted for the Run 1 data.

TABLE I. Results of the individual counts N , acceptance ratio R_Ω , and $Br(K_{e2\gamma}^{\text{SD}})/Br(K_{e2})$ values with statistical uncertainties obtained by simultaneously fitting the events with 1-cluster, 2-cluster, and without CsI(Tl) constraint for Run 1 and Run 2. An error-weighted average of the Run-1 and Run-2 results was adopted as the final result.

	Run period	Run 1	Run 2	Combined
Without CsI(Tl) constraint	$N(K_{e2})$	2344 ± 55	306 ± 20	2650 ± 59
1 cluster	$N(K_{e2\gamma})$	437 ± 24	49 ± 8	486 ± 28
	R_Ω	6.58	6.85	
2 cluster	$N(K_{e2\gamma})$	78 ± 4	8 ± 2	86 ± 4
	R_Ω	36.8	44.8	
Results	χ^2/dof	39.2/43	43.1/43	
	$N(K_{e2\gamma})$	515 ± 28	57 ± 9	572 ± 29
	$Br(K_{e2\gamma}^{\text{SD}})/Br(K_{e2})$	1.24 ± 0.07	1.1 ± 0.2	1.22 ± 0.07

The e^+ momentum spectra were obtained using the same PID condition for events with the 1-cluster, 2-cluster, and without CsI(Tl) constraint events are shown in Fig. 7 (a), (b), and (c), respectively, indicated by the dots. The $Br(K_{e2\gamma}^{\text{SD}})/Br(K_{e2})$ ratio was derived to be 1.1 ± 0.2 , which is consistent with the result using the Run 1 data in spite of the larger number of $K_{\mu 2}$ background events. The solid (green), dashed (blue), and dashed-dotted (magenta) lines in Fig. 7 are the $K_{e2\gamma}$, K_{e2} , and $K_{\mu 2}$ decays, respectively, obtained by the simulation calculation. The thick-red line is the fitted result obtained by adding all the decay contributions. The details of the analysis result are summarized in Table I. In addition to the Run 2 analysis described above, a separate study was performed with the Run 1 data. The cuts were tightened to remove the $K_{\mu 2}$ backgrounds more strictly and relaxed to accept the genuine $K_{e2\gamma}$ events with higher efficiency, although the statistical uncertainties were significantly enlarged. The $Br(K_{e2\gamma})/Br(K_{e2})$ values determined by these PID conditions were consistent with those obtained using the optimized PID conditions within uncertainties, indicating a good reproducibility of the PID analysis in the simulation.

In the present work, the $Br(K_{e2\gamma}^{\text{SD}})$ value relative to $Br(K_{e2})$ was obtained by calculating the ratio of the $K_{e2\gamma}$ and K_{e2} yields. The charged particle analysis was common for the two decays, while the photon measurement was only required for the $K_{e2\gamma}$ selection. Therefore, the dominant contributions to the systematic uncertainty are due to the ambiguity of the

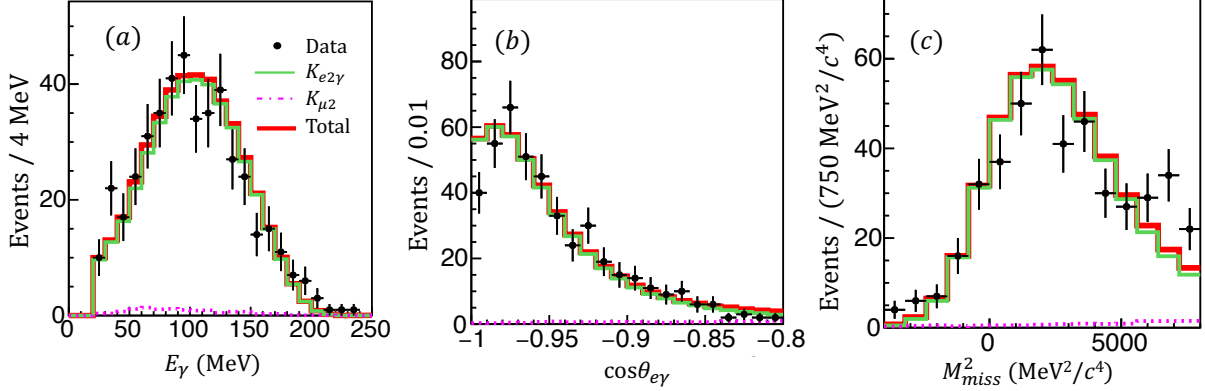


FIG. 6. The $K_{e2\gamma}$ spectra with the 1-cluster requirement: (a) E_γ , (b) $\cos\theta_{e\gamma}$, and (c) M_{miss}^2 . The $K_{e2\gamma}$ events were selected by imposing $p > 230$ MeV/ c , $-4000 < M_{\text{miss}}^2 < 8000$ MeV $^2/c^4$, and $\cos\theta_{e\gamma} < -0.8$ to suppress the K_{e3} and $K_{\mu2}$ contributions. The black dots are the experimental data. The solid (green) and dashed-dotted (magenta) histograms are the simulation data of $K_{e2\gamma}$ and $K_{\mu2}$ with accidental backgrounds, respectively. The thick-red line is the total simulation result obtained by adding each component.

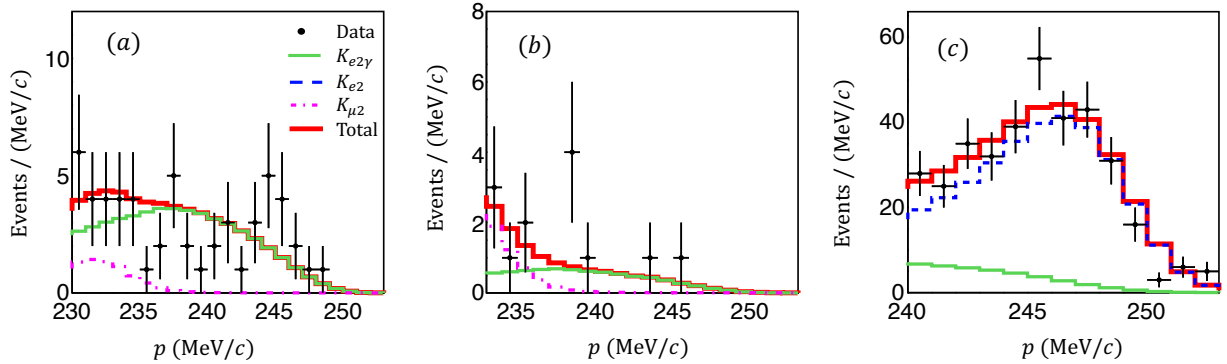


FIG. 7. Charged particle momentum spectra for the Run 2 data with requiring the (a) 1-cluster and (b) 2-cluster in the CsI(Tl) calorimeter and (c) without CsI(Tl) constraint. The black dots are the experimental data. The solid (green), dashed (blue), and dashed-dotted (magenta) lines are the $K_{e2\gamma}$, K_{e2} , and $K_{\mu2}$ decays, respectively, determined by simulation calculations. The thick-red lines are the fitted result obtained by adding all decay contributions.

radiative photon measurement in the $K_{e2\gamma}$ decay. The systematic uncertainties for the $Br(K_{e2\gamma}^{\text{SD}})/Br(K_{e2})$ determination are summarized in Table II.

The imperfect reproducibility of the CsI(Tl) hole structure aligned with the 12 spectrometer gaps in the simulation can introduce a systematic uncertainty through a change in the

TABLE II. Summary of the systematic uncertainties for the $Br(K_{e2\gamma}^{\text{SD}})/Br(K_{e2})$ ratio determination.

Source	Systematic uncertainty
Hole size of CsI(Tl) calorimeter	0.017
CsI(Tl) misalignment	< 0.001
Imperfect reproducibility of photon angular distribution	< 0.001
Accidental backgrounds in CsI(Tl)	0.004
Photon energy threshold of CsI(Tl)	0.007
Photon energy calibration of CsI(Tl)	< 0.001
Photon timing window	0.009
CsI(Tl) detection efficiency	0.012
AC detection efficiency	0.007
PGC detection efficiency	0.007
TOF detection efficiency	0.019
$K_{\mu 2}$ background subtraction	0.015
$K_{e2\gamma}^{\text{SD}}$ form factor	0.011
K^+ stopping distribution	0.003
Material thickness in the central parts	< 0.001
Positron momentum resolution	0.002
Magnetic field	0.002
In-flight kaon decay	0.002
Total	0.036

photon acceptance. This effect was estimated by considering the maximum conceivable hole size change of 2 mm. Since the accidental backgrounds were concentrated in the energy region below 30 MeV, these events are very sensitive to the photon energy cut point. The cut point was changed from 18 MeV to 30 MeV, and the $Br(K_{e2\gamma}^{\text{SD}})/Br(K_{e2})$ change was interpreted as the uncertainty from this cut point effect. Although the CsI(Tl) accidental backgrounds were taken into account in the simulation, the CsI(Tl) timing window was relaxed to accept more accidental events. The timing window of ± 50 ns was intentionally increased up to ± 60 ns, and the $Br(K_{e2\gamma}^{\text{SD}})/Br(K_{e2})$ change was adopted as the systematic uncertainty. To check effects from the background intensity fluctuation, the beam back-

ground data obtained using the $K_{\mu 2}$ events were separated into 4 subsets using time series of the experimental period and $Br(K_{e 2\gamma}^{\text{SD}})/Br(K_{e 2})$ was determined for each background sample. The variance of the average value was used to estimate this effect.

The momentum dependence of the PID detectors from 200 to 250 MeV/ c was measured using the $K_{e 3}$ and in-flight $K_{e 3}$ events and taken into account in the simulation. However, its statistical uncertainty introduced a possible change in the efficiency correction, which was regarded as a systematic effect in the efficiency correction. Also, the statistical uncertainty of the CsI(Tl) efficiency obtained using the $K_{\pi 2}$ events was treated as a systematic effect of the photon measurement by the CsI(Tl) calorimeter. The E36 simulation started from K^+ decays at rest and we did not take into account in-flight K^+ decay in the simulation. The fraction of the in-flight decays was changed by the TOF1 timing cut, and the parameter shifts were interpreted as this effect. Because the $K_{\mu 2}$ backgrounds were subtracted from the observed $K_{e 2}$ and $K_{e 2\gamma}$ samples, a mis-understanding of the response function for the $K_{\mu 2}$ momentum determination would introduce a systematic uncertainty. This effect was estimated by changing the PID conditions around the selected windows.

Since the (e^+, γ) angular correlation and photon energy distributions depend on the $K_{e 2\gamma}$ form factor, the detector acceptance was affected by the λ parameter. The $Br(K_{e 2\gamma}^{\text{SD}})/Br(K_{e 2})$ shift due to a parameter change of $\Delta\lambda = 0.1$ [3] was interpreted as the systematic uncertainty. In addition, effects from a misunderstanding of the K^+ stopping distribution and TGT thickness, inaccuracy of the K^+ vertex position and e^+ momentum determinations, etc. were evaluated, but these effects were common for the $K_{e 2}$ and $K_{e 2\gamma}$ decays and cancelled out in their ratio. The total size of the systematic uncertainty in the $Br(K_{e 2\gamma}^{\text{SD}})/Br(K_{e 2})$ determination was thus obtained by adding each item in quadrature to be 0.036.

The $K_{e 2\gamma}$ branching ratio relative to the $K_{e 2}$ decay was determined using the Run 1 and Run 2 analysis results with the number of the $K_{e 2\gamma}$ events of 572 ± 29 , and an error-weighted average of these values was adopted as the final result by adding the total size of the systematic uncertainties as, $Br(K_{e 2\gamma}^{\text{SD}})/Br(K_{e 2}) = 1.22 \pm 0.07_{\text{stat}} \pm 0.04_{\text{syst}}$. The $Br(K_{e 2\gamma}^{\text{SD}})$ value relative to the $K_{\mu 2}$ decay can be expressed as,

$$\frac{Br(K_{e 2\gamma}^{\text{SD}})}{Br(K_{\mu 2})} = \frac{Br(K_{e 2\gamma}^{\text{SD}})}{Br(K_{e 2})} \times \frac{Br(K_{e 2})}{Br(K_{\mu 2})} = \frac{Br(K_{e 2\gamma}^{\text{SD}})}{Br(K_{e 2})} \times R_K^{\text{SM}} \quad (4)$$

using the R_K^{SM} prediction. Therefore, the $Br(K_{e 2\gamma}^{\text{SD}})/Br(K_{\mu 2})$ value is derived to be $(3.02 \pm 0.17_{\text{stat}} \pm 0.10_{\text{syst}}) \times 10^{-5}$. Next, the partial fraction of the $K_{e 2\gamma}^{\text{SD}}$ branching ratio in the phase space region ($p > 200$ MeV/ c , $E_\gamma > 10$ MeV) is obtained by correcting for the phase space

reduction as,

$$\frac{Br(K_{e2\gamma}^{\text{SD}}, p > 200 \text{ MeV}/c, E_\gamma > 10 \text{ MeV})}{Br(K_{\mu 2})} = (2.01 \pm 0.11_{\text{stat}} \pm 0.07_{\text{syst}}) \times 10^{-5}. \quad (5)$$

This is significantly larger than the result, $(1.483 \pm 0.066_{\text{stat}} \pm 0.011_{\text{syst}}) \times 10^{-5}$, reported in the previous experimental study [8] which supported one of the theoretical models of ChPT- $\mathcal{O}(p^6)$ [11].

We would like to express our gratitude to all member of the J-PARC Accelerator, Cryogenic, and Hadron Experimental Facility groups for their support. The present work was supported by JSPS KAKENHI Grant numbers JP26287054, JP15K05113, JP22340059, and JP23654088 in Japan; by NSERC (SAPPJ-2017-00034) and NRC (TRIUMF) in Canada; by Department of Energy (DOE) DE-SC0003884, DE-SC0013941, US National Science Foundation (NSF) PHY-1505615 in the United States; and by Russian Science Foundation Grant No. 14-12-00560 in Russia.

-
- [1] P. A. Zyla et al. (Particle Data Group), Prog. Theor. Exp. Phys. 2020, 083C01 (2020).
 - [2] J. Bijnens, G. Colangelo, G. Ecker, and J Gasser, published in 2nd DAPHNE Physics Handbook, 315.
 - [3] V. Cirigliano et al., Review of Modern Physics 84 (2012) 399.
 - [4] W. J. Marciano and A. Sirlin, Phys. Rev. Lett. 71 (1993) 3629.
 - [5] F. Finkemeier, Phys. Lett. B 387 (1996) 391.
 - [6] V. Cirigliano and I. Rosell, Phys. Rev. Lett. 99 (2007) 231801.
 - [7] A. Masiero, P. Paradisi, and R. Petronzio, J. High Energy Phys. 0811 (2008) 042.
 - [8] F. Ambrosino et al., Eur. Phys. J. C 64 (2009) 627; Eur. Phys. J. C 65 (2010) 703.
 - [9] C. Lazzeroni et al., Phys. Lett. B 719 (2013) 326.
 - [10] C. Q. Geng, I-Lin Ho, and T. H. Wu, Nucl. Phys. B 684 (2004) 281.
 - [11] Chuan-Hung Chen et al., Phys. Rev. D 77 (2008) 014004.
 - [12] S. Shimizu, et al., Proposal for J-PARC 50 GeV Proton Synchrotron, P36 June, 2010; http://j-parc.jp/researcher/Hadron/en/Proposal_e.html
 - [13] S. Strauch et al., Proc. Sci., PoS(KAON13)014, 2013.
 - [14] A. Kawachi et al., Nucl. Instr. and Meth. A 416 (1998) 253.
 - [15] D. V. Dementyev et al., Nucl. Instr. Meth. A 440 (2000) 151.

- [16] J. A. Macdonald et al., Nucl. Instr. Meth. A 506 (2003) 60.
- [17] M. Abe et al., Phys. Rev. D 73 (2006) 072005.
- [18] S. Shimizu et al., Phys. Lett. B 495 (2000) 33; Y. H. Shin et al., Eur. Phys. J. C 12 (2000) 627; K. Horie et al., Phys. Lett. B 513 (2001) 311; M. A. Aliev et al., Phys. Lett. B 554 (2003) 7; S. Shimizu et al., Phys. Rev. D 70 (2004) 037101; S. Shimizu et al., Phys. Lett. B 633 (2006) 190.
- [19] V. Fitch and R. Motley, Phys. Rev, 101 (1956) 496.
- [20] O. Mineev et al., Nucl. Instr. Meth. A 847 (2017) 136.
- [21] M. Tabata et al., JPS Conf. Proc. 8, 024001 (2015).
- [22] M. Tabata et al., Nucl. Instr. Meth. A 795 (2015) 206.
- [23] Y. Miyazaki et al., Nucl. Instr. Meth. A 779 (2015) 13.
- [24] <https://www.triumf.info/wiki/DAQwiki/index.php/VF48>; Y. Igarashi and M. Saito, in: IEEE 2012 Nuclear Science Symposium and Medical Imaging Conference Record (Nss/MIC).
- [25] H. Ito et al., Nucl. Instr. Meth. A 901 (2018) 1.